



# Determining the optimal thin layer height for single-station ionospheric modeling and its influence on the estimation of DCB

Hui Xi<sup>1</sup> · Hu Jiang<sup>2</sup> · Jiachun An<sup>3,4</sup> · Na Cheng<sup>2</sup> · Tianyang Bai<sup>5</sup> · Jingxue Bi<sup>2</sup>

Received: 30 December 2023 / Accepted: 23 May 2024 / Published online: 31 May 2024  
© The Author(s), under exclusive licence to Springer-Verlag GmbH Germany, part of Springer Nature 2024

## Abstract

The thin layer ionospheric height (TLIH) is a crucial parameter of the mapping function (MF), directly impacting the accuracy of converting slant total electron content (TEC) to vertical TEC. Due to the complex spatio-temporal variations in ionospheric space gradients, a fixed TLIH is inadequate in reflecting the true changes in ionospheric TEC. In this study, we propose an improved dG-TLIH technique to effectively model single-station ionospheric TEC. Additionally, we analyze the spatio-temporal variation characteristics of TLIH and its influence on single-station ionospheric TEC modeling, as well as the estimation of satellite and receiver differential code biases (DCBs). Experimental results demonstrate the following: (1) The “true” mapping value is closely related to latitude and local time. Even when the elevation angle reaches 30°, the difference in mapping values between different ionospheric states could reach 0.2. (2) The thin layer height exhibits distinct diurnal variations, with peak and trough occurrences at local times in various latitude regions. (3) Compared to the fixed height of 450 km, the ionospheric models based on the dG-TLIH technique show improvements of 16.3% at low latitudes, 9.6% at middle latitudes, and 14.8% at high latitudes. (4) The utilization of the dG-TLIH technique enhances the satellite and receiver DCB values by an average of 6.7–20.8% and 7.6–15.5%, respectively.

**Keywords** Thin layer ionospheric height (TLIH) · Mapping function (MF) · Total electron content (TEC) · Ionospheric modeling · Differential code bias (DCB)

## Introduction

The ionosphere contains a large number of free electrons, which can have various impacts on communication and broadcast electromagnetic signals that pass through it. These impacts include reflection, refraction, scattering, and absorption. When it comes to navigation signals broadcasted by global navigation satellite systems (GNSS), the ionosphere

can cause a range delay of several meters or even hundreds of meters (Hernández-Pajares et al. 2011; Jin et al. 2022; Komjathy 1997). This delay can significantly reduce the accuracy and reliability of satellite navigation positioning (Macalalad et al. 2014). In fact, it is the most significant source of error that affects the performance of GNSS positioning, navigation, and timing (PNT) applications (Liu et al. 2016; Rovira-Garcia et al. 2015).

Total electron content (TEC) is one of the most important quantitative parameters of the earth’s ionosphere, and the ionospheric delay is directly proportional to it. Fortunately, based on the dispersion effect of the ionosphere and GNSS dual-frequency or multi-frequency observation data, we can use the carrier-to-code levelling (CCL) or uncombined precise point positioning (UPPP) method to invert the TEC observation values (Liu et al. 2011; Zhang 2016). However, GNSS-derived ionospheric observables not only contain TEC information, but also satellite and receiver differential code biases (DCBs). To separate these DCBs from the TEC, ionospheric TEC modeling is necessary (Li et al. 2014; Sasibhushana Rao 2007; Shi et al. 2016).

✉ Hu Jiang  
jianghu0429@163.com

<sup>1</sup> College of Geography and Environment, Shandong Normal University, Jinan, China  
<sup>2</sup> School of Surveying and Geo-Informatics, Shandong Jianzhu University, Jinan, China  
<sup>3</sup> Chinese Antarctic Center of Surveying and Mapping, Wuhan University, Wuhan, China  
<sup>4</sup> Key Laboratory of Polar Environment Monitoring and Public Governance, Wuhan University, Ministry of Education, Wuhan, China  
<sup>5</sup> State Grid Siji Location Service Co., Ltd, Beijing, China

In the field of GNSS PNT applications, the thin layer ionospheric model (TLIM) is widely used due to its simplicity and ease of use (Jiang et al. 2019; Jin et al. 2022; Li et al. 2015; Liu et al. 2014; Xi et al. 2020). It shares a common assumption that all free electrons of the ionosphere are contained in a layer of infinitesimal thickness at a given reference altitude (Schaer 1999). The thin layer ionospheric height (TLIH) is one of the key parameters of the TLIM, as it affects the position of the ionospheric puncture point (IPP), the mapping function, and the accuracy of ionospheric modeling (Jiang et al. 2018; Nava et al. 2007). Currently, TLIHs of the TLIM are mainly selected based on experience. The GPS Klobuchar model uses a TLIH of 350 km (Klobuchar 1987), the BeiDou Klobuchar-like model uses a TLIH of 375 km, the BDGIM model of the BeiDou-3 uses a TLIH of 400 km (Yuan et al. 2019), and the GIM product provided by IGS uses a TLIH of 450 km (Hernández-Pajares et al. 2011). Wide area augmentation systems also establish ionospheric TEC grid models with a TLIH of 350 km (Krankowski et al. 2009).

However, the TLIH is affected by the spatial gradient of the ionospheric plasma, which changes with time, solar activity, latitude, and other factors, and is not a fixed height (Chen et al. 2022; Jiang et al. 2018). Many researchers have proposed methods for extracting the optimal TLIH and analyzed the spatio-temporal changes of the optimal TLIH, as well as its impact on ionospheric modeling and differential code bias (DCB) estimation. Birch et al. (2002) proposed an inverse method that uses simultaneous vertical and slant TEC observations to estimate the effective shell height. Li et al. (2018) analyzed the spatio-temporal variation of the optimal TLIH in China, and the results showed that the optimal TLIH ranges from 450 to 550 km in China. Xiang and Gao (2019) used the equal integration method to obtain the optimal TLIH based on a three-dimensional ionospheric model and analyzed its impact on single-station ionospheric modeling and DCB estimation. The results showed that the optimal TLIH can reduce mapping error by 35%, and its impact on the receiver DCB can reach 1.0 ns. Zhao and Zhou (2018) analyzed the periodicity of the optimal thin-layer height of each station and its impact on single-station modeling based on five GNSS observation stations at different latitudes. The results showed that the optimal TLIH varied greatly at different latitudes, with annual and solar cycle variations, which could improve the average error by 50–88%. Jiang et al. (2021) proposed the dG-TLIH technique for detecting the optimal TLIH based on the dSTEC (differential STEC) measurements and the UQRG (UPC quarter-of-an-hour rapid GIM) GIMs and analyzed the characteristics of the optimal TLIH variation in the Arctic and Antarctic. The results show that the optimal TLIH is related to solar variation, with seasonal and annual cycle changes in the Arctic and Antarctic. Xu et al. (2023) presented a flexible IEH solution based on

neural network models and applied it to global ionospheric TEC modeling.

The remainder of this contribution is organized as follows: Sect. "Materials and methods" introduces the calculation method of the optimal TLIH, the modeling method of the single-station ionospheric model, the DCB estimation method, and the data sources used. Sect. "Results and discussion" analyzes the characteristics of the spatio-temporal variation of the mapping values and optimal TLIH. Section 4 presents the accuracy evaluation of ionospheric models and DCB based on different TLIHs. Finally, Sect. "Summary and conclusion" provides concluding remarks.

## Materials and methods

In this section, we provide a detailed description of the determination method for TLIH, estimation method for DCB, and observation data used in the experiments.

### Optimal TLIH calculation

This study utilizes the dG-TLIH technique (Jiang et al. 2021) to calculate the optimal TLIH for each observation station. The calculation is based on the dSTEC measurements and UQRG-GIMs. Along a phase-continuous satellite-receiver arc, the dSTEC measurements can be expressed as follows:

$$dSTEC(t) = STEC_r^s(t) - STEC_r^s(t_{E_{\max}}) = \frac{1}{\mu} (\phi_{r,GF}^s(t) - \phi_{r,GF}^s(t_{E_{\max}})) \quad (1)$$

where  $STEC_r^s(t)$  denotes the ionospheric total electron content (TEC) on the slant path from satellite  $s$  to receiver  $r$  at time  $t$ ;  $t_{E_{\max}}$  denotes the maximum satellite elevation in a continuous satellite-receiver arc of measurements;  $\mu = 40.3 \times 10^{16} \times (f_2^{-2} - f_1^{-2})$  is a frequency  $f$  dependent conversion factor;  $\phi_{GF} = \phi_1 - \phi_2$  is the geometry-free combination of the carrier phase. Since the dSTEC measurements is calculated from carrier-phase observations, its accuracy is less than 0.1 TECU.

Within a common arc of measurements for each given pair of satellites and receivers, the STEC at the given time  $t$  can be expressed as:

$$STEC(t) = STEC(t_{E_{\max}}) + dSTEC(t) \quad (2)$$

where the definitions of the variables in (2) are the same as that in (1).

Indeed, the "true" mapping value at the given time  $t$  can be expressed as

$$MV_T(t) = \frac{STEC(t)}{VTEC(t)} = \frac{VTEC(t_{E_{\max}}) \cdot mf(E_{\max}) + dSTEC(t)}{VTEC(t)} \quad (3)$$

where  $VTEC(t_{E_{max}})$  and  $VTEC(t)$  are the vertical TEC at the moment of maximum elevation and  $t$  within a continuous satellite–receiver arc, respectively, calculated using UQRG-GIM;  $mf(E) = \frac{1}{\sqrt{1-(R \cos(E)/(R+H))^2}}$  denotes the mapping

$$\widetilde{TEC}_i = -\frac{1}{\mu} \left( \phi_{GF}^i - \frac{\sum_{i=1}^k (\phi_{GF}^i + P_{GF}^i)}{k} - c(\text{DCB}_r + \text{DCB}^s) \right) + \varepsilon_{\widetilde{TEC}} \tag{5}$$

function,  $R$  is the average radius of the Earth,  $H$  is the TLIH. To reduce the influence of the ionospheric gradients, only the continuous arc segments with the maximum elevation angle greater than  $60^\circ$  are used in this study. From this equation, it can be seen that the “true” mapping value is related to TLIH.

The dSTEC retrieved from GPS, BDS, GLONASS and Galileo measurements are used to estimate the  $MV_T$  in a 2-h moving window with 1-h step at each selected GNSS station. Therefore, the mapping function error indicator at a given TLIH can be expressed as:

$$\sigma_H = \sqrt{\frac{1}{n} \sum_{i=1}^n (MV_T(t_i) - mf_H(E_i))^2} \tag{4}$$

$$\begin{cases} STEC(\varphi, \lambda, t) = VTEC(\varphi, \lambda, t) \cdot mf_H(E) \\ VTEC(\varphi, \lambda, t) = \sum_{n=0}^{n_{max}} \sum_{m=0}^{m_{max}} A_{nm} \varphi^n h^m + \sum_{k=0}^{k_{max}} (B_k \cos(kh) + C_k \sin(kh)) \\ \varphi_m = \varphi + 0.064 \cos(\lambda - 1.617) \\ h = 2\pi(t - 14)/T, T = 24 h \end{cases} \tag{6}$$

where  $n$  is the total number of samples;  $MV_T(t_i)$  denotes the mapping value calculated by Eq. (3) at time  $t_i$ ;  $E_i$  is the satellite elevation; and  $mf_H$  denotes the mapping function with the TLIH of  $H$ . Based on the different TLIH settings, the mapping function error indicator of each observation station at different time periods can be calculated, and then the TLIH corresponding to the minimum  $\sigma_H$  can be selected as the optimal TLIH (OTLIH).

### Deriving TEC from GNSS measurements

According to the dispersion characteristics of the ionosphere on radio signals, the ionospheric delay of radio signals is a function of the signal frequencies, and the ionospheric TEC corresponds to the total number of electrons along a satellite–receiver path. Unfortunately, TEC observations derived from the geometry-free combination of pseudo-range measurements suffer from noise and

multipath effects. While carrier phase measurements have high accuracy, it is challenging to eliminate unknown integer phase ambiguities. Therefore, a carrier-to-code leveling (CCL) approach (Ciraolo et al. 2007) was used to derive the ionospheric TEC observations as follows:

where  $P_{GF} = P_1 - P_2$  is the geometry-free combination of the pseudo-range measurements;  $k$  is the smoothing length;  $c$  is the speed of light;  $\text{DCB}_r$  and  $\text{DCB}^s$  represent the receiver and satellite differential code bias (DCB).

### Ionosphere Modeling and DCB Estimation

It should be noted that the GNSS-derived TEC is also affected by satellite and receiver DCBs. In this paper, the IGGDCB (IGG, Institute of Geodesy and Geophysics) method (Li et al. 2012; Wang et al. 2016) is used to calculate the satellite and receiver DCBs. To separate the “pure” TEC from the DCB, the generalized triangular series function (GTSF) (Yuan and Ou 2004) was introduced to model the local ionospheric vertical TEC at each GNSS station, as shown in (6).

where  $VTEC(\varphi, \lambda, t)$  is the VTEC at the IPP  $(\varphi, \lambda)$  at time  $t$ ;  $n_{max}$  and  $m_{max}$  denote the maximum degrees of the polynomial development and  $k_{max}$  is the maximum degree of the

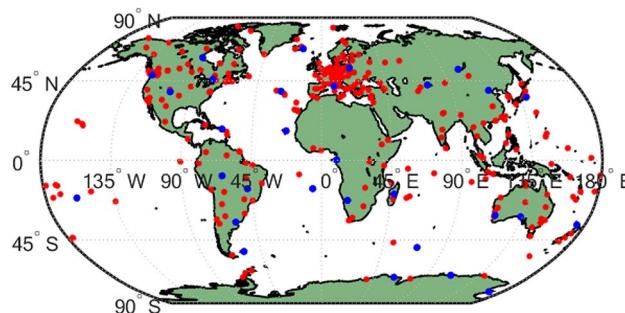


**Fig. 1** The geographical locations of GNSS ground stations. The red dots are used to estimate DCB, and the blue dots are used to evaluate ionospheric models

finite Fourier series; the  $n_{\max}$ ,  $m_{\max}$  and  $k_{\max}$  are set as 2, 2 and 5, respectively;  $\varphi_m$  and  $h$  are geomagnetic latitude and solar longitude of the IPP, respectively.

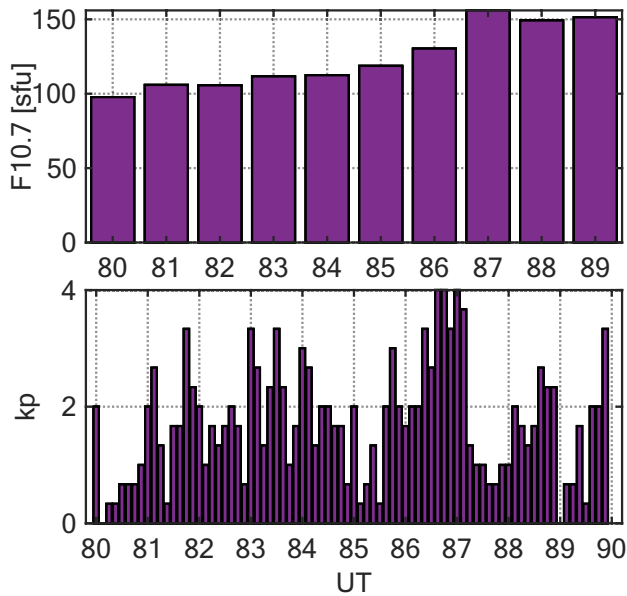
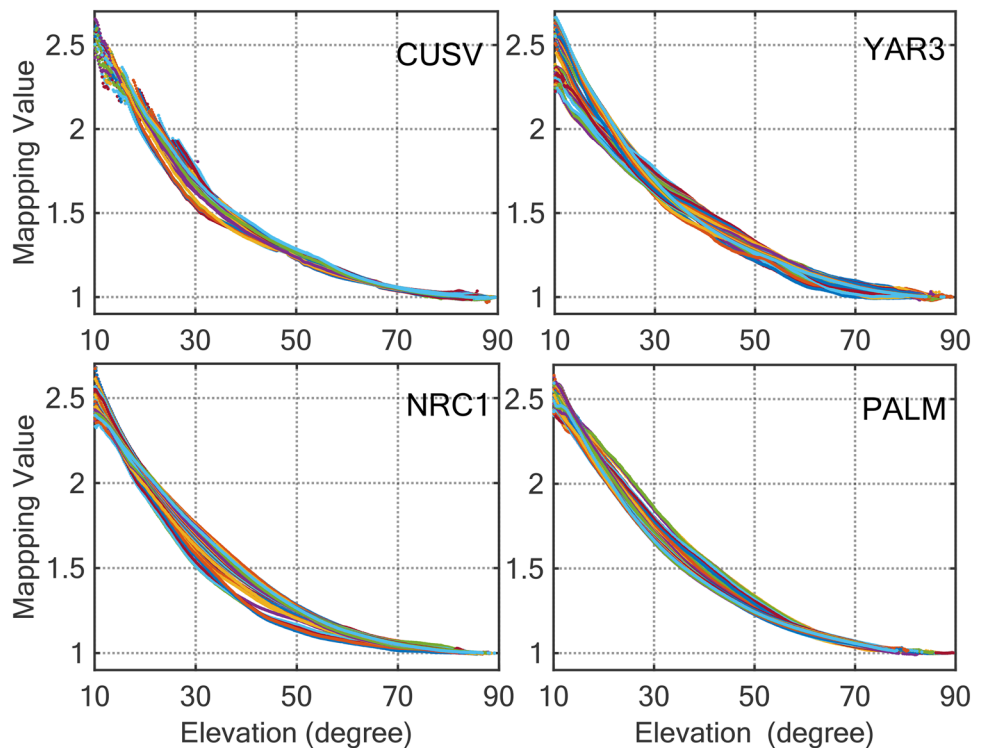


**Fig. 2** Solar activity index F10.7 (top) and geomagnetic activity index kp (bottom) from DOY 80 to 89 in 2022

**Fig. 3** Variation of the mapping values computed by Eq. (3) against elevation angles at different times of the day (DOY 82, 2022) from four stations in different latitudes



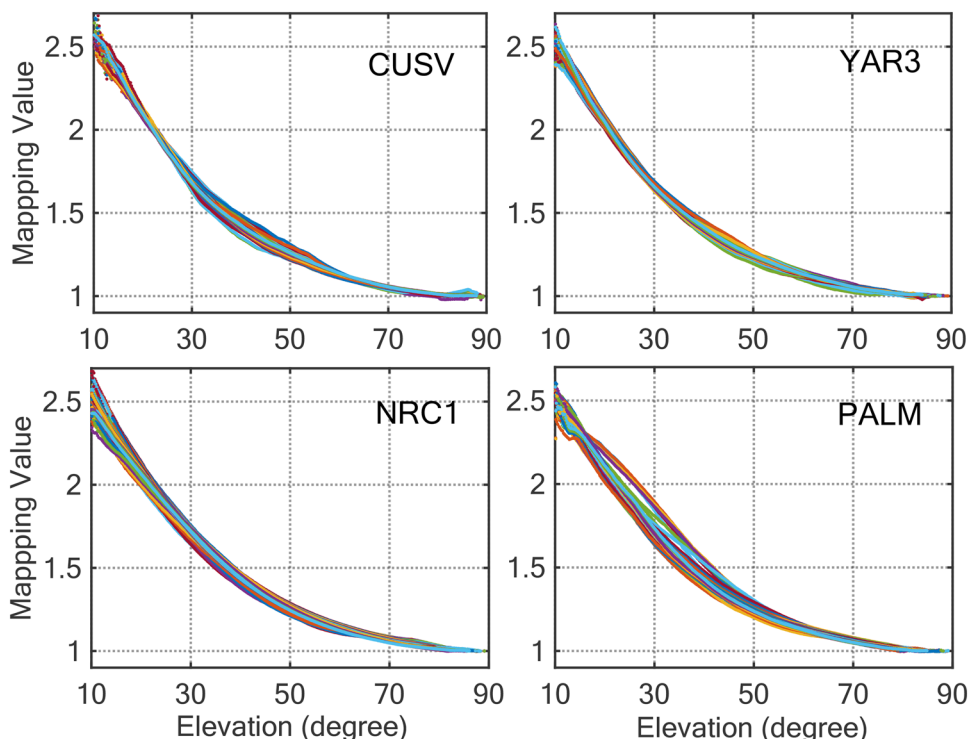
### Observation Data

A network of 170 MGEX stations worldwide was selected for data analysis and new algorithm evaluation. Among these, 140 stations were used to estimate DCB, while the remaining 30 stations were used to assess the accuracy of the ionospheric TEC model. The distribution of these 170 stations is displayed in Fig. 1. To validate the algorithm, ten days of GPS, BDS, GLONASS, and Galileo observation data were collected at 30-s intervals from DOY (day of year) 80 to 89 in 2022. Figure 2 shows the time series of the solar activity index F10.7 and the geomagnetic activity index kp (<https://wdc.kugi.kyoto-u.ac.jp>). It can be observed that the F10.7 index ranged from 100 to 150 sfu, and the kp index remained within 4.

### Mapping value and optimal TLIH from dG-TLIH technique

As mentioned previously, the dG-TLIH technique was applied to generate station-specific mapping values and optimal TLIH with a 1-h step. To illustrate the spatio-temporal variation characteristics of these mapping values, we selected four observation stations from different latitude regions. Figures 3 and 4 depict the variation of the mapping values, computed using Eq. (3), against elevation angles at four observation stations (CUSV: 13.7°, 100.5°; YAR3: -29.0°, 115.3°; NRC1: 45.4°, -75.6°; PALM: -64.8°, -64.0°) on DOY 82 and 86 of 2022, respectively. The different-colored lines

**Fig. 4** Variation of the mapping values computed by (3) against elevation angles at different times of the day (DOY 86, 2022) from four stations in different latitudes



represent the mapping values at different periods (using a 2-h moving window with a 1-h step) throughout the day. The "true" mapping values exhibit significant variations across different latitudes and times. On DOY 82 (F10.7: 105.6 sfu) of 2022, the mapping values of the YAR3 station showed significant differences across different time periods, even when the elevation angle reached 70°. The mapping values of the NRC1 station displayed the largest daily difference

at an elevation angle of approximately 40°. The mapping values of the CUSV and PALM stations tended to remain consistent when the elevation angles exceeded 50°. However, on DOY 86 in 2022, apart from the PALM station, the differences in mapping values across different time periods decreased compared to the DOY 82.

To better illustrate the differences in mapping values between different time periods, we calculated the

**Fig. 5** The differences between the mapping values computed by Eq. (3) and mapping function based on 450 km at different times of the day (DOY 82, 2022) from four stations in different latitudes

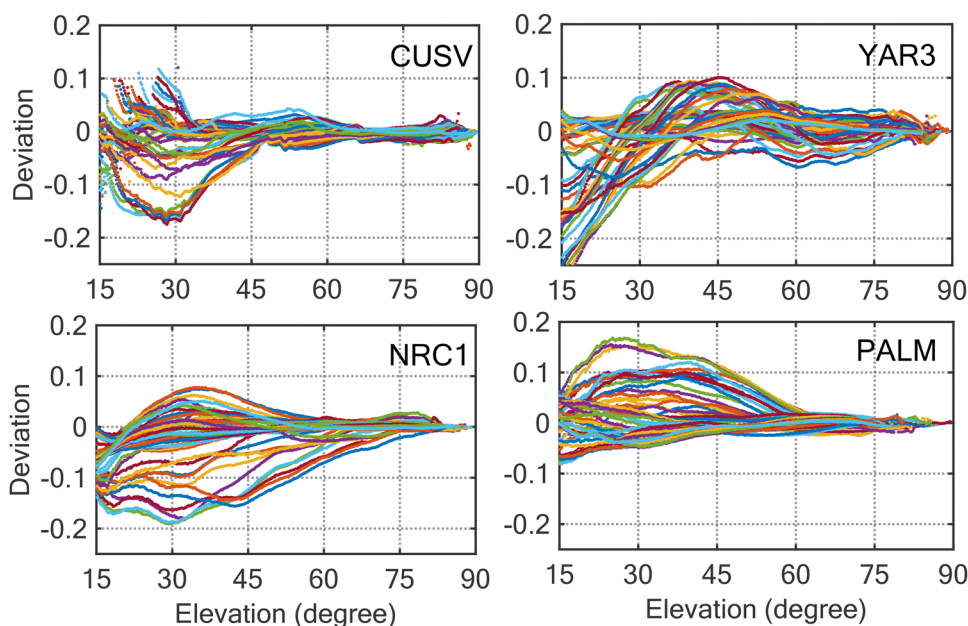




**Fig. 6** The differences between the mapping values computed by Eq. (3) and mapping function based on 450 km at different times of the day (DOY 86, 2022) from four stations in different latitudes

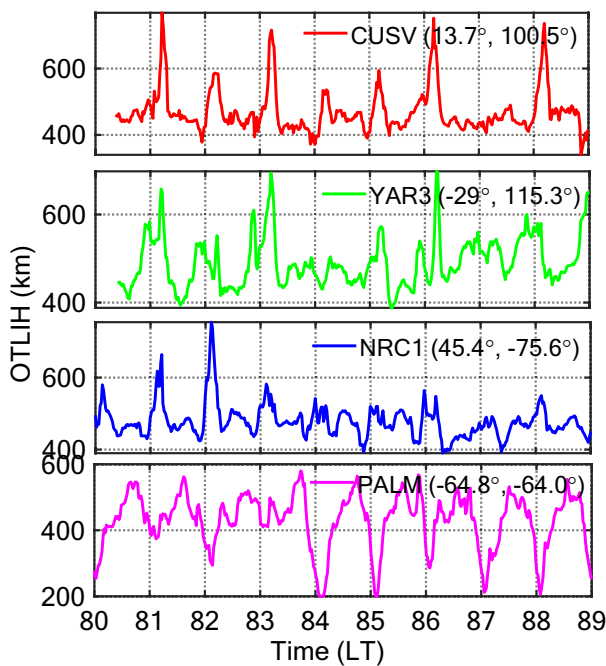
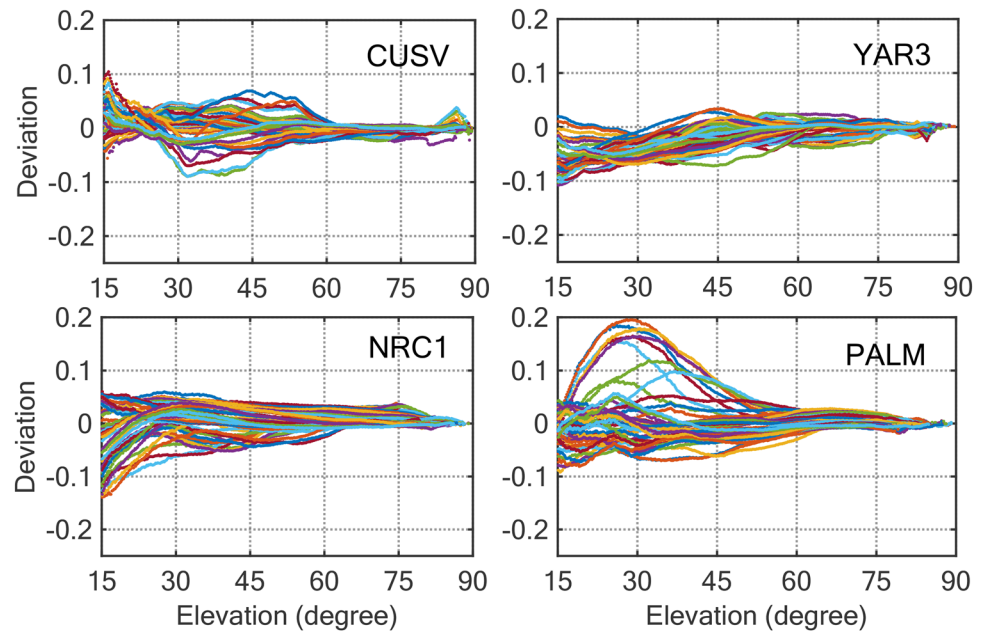


**Fig. 7** Station-specific variation of the TLIH based on dG-TLIH technique against the local time during DOY 80 to 89 in 2022 at four stations in different latitudes

discrepancies between the mapping values computed by the dG-TLIH technique and the mapping function based on the fixed TLIH of 450 km. These differences are shown in Figs. 5 and 6. From these two figures, it is evident that the discrepancy in mapping values can reach 0.2. What is more

surprising is that at certain stations (YAR3, PALM, NRC1), the deviation in mapping values during specific periods can even reach 0.1, even when the elevation angle reaches  $40^\circ$ . Hence, relying solely on a fixed TLIH proves challenging in capturing the "true" mapping value.

Figure 7 shows the station-specific variation of the TLIH based on the dG-TLIH technique against local time during DOY 80 to 89 in 2022 at four stations located in different latitudes. It can be observed that the TLIH exhibits significant diurnal cycles, with variations of up to 500 km (ranging between 200 and 700 km) within a day at different locations and times. It decreases during the day, especially after sunrise when photoionization begins. On the contrary, TLIH that begins before and after sunset, when recombination becomes more dominant compared to F2 photoionization, increases and reaches its peak between 4:00 and 5:00. However, different variations are observed in the polar regions (station: PALM). TLIH reaches its peak around 17:00 and hits a trough around 2:00. This phenomenon may be associated with the Weddell Sea Anomaly, a distinctive ionospheric occurrence unique to the Antarctic Peninsula and Weddell Sea regions during local summer (Horvath 2006). It is distinguished by a notable enhancement in night-time (18:00–02:00 LT) electron density, an effect that surpasses the electron density levels observed during the daytime (08:00–18:00 LT). This also suggests that the method is capable of capturing the unique spatiotemporal variations in the local ionosphere and effectively addressing the limitations of the thin-layer model.

## Results and discussion

In this section, we will analyze the impact of TLIH on single-station ionosphere modeling, satellite and receiver DCB estimation through specific experiments.

### TLIH impacts on ionospheric modeling

According to the principle of the IGGDCB algorithm, it is known that the estimation accuracy and reliability of DCB depend on the accuracy of single-station ionospheric TEC modeling. In this study, we used the generalized triangular series function to map the diurnal TEC variation through a set of parameters at each GNSS station. We adopted a 19-parameter GTS function (polynomial order:  $n_{max} = m_{max} = 2$ , triangular series order:  $k_{max} = 4$ ) to map the single-station diurnal TEC, based on the Earth-fixed geomagnetic coordinate system.

In order to analyze the comprehensive performance of the ionospheric model in different latitudes, we calculate the bias, RMS of the ionospheric model based on different TLIHs (450 km and dG-TLIH) at high latitudes ( $\pm 60^\circ \sim \pm 90^\circ$ , 6 stations), middle latitudes ( $\pm 30^\circ \sim \pm 60^\circ$ , 15 stations) and low latitudes ( $0^\circ \sim \pm 30^\circ$ , 9 stations), as shown in Fig. 8. As shown in the Figure, the accuracy of the ionosphere model constructed using the TLIH determined

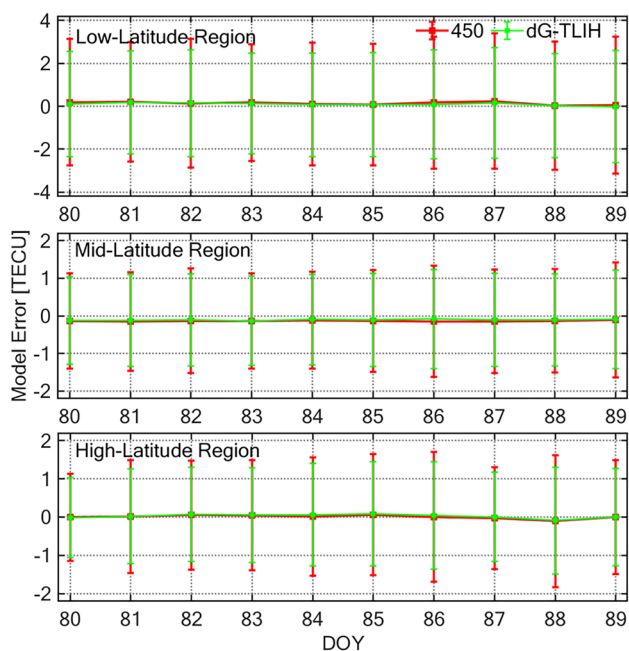


**Fig. 8** The error bar of the ionospheric TEC model constructed using single station modeling based on GTS function during DOY 80 to 89 in 2022. The red bar represents the results using the TLIH of 450 km and the green bar represents the results using the TLIH from dG-TLIH technique

based on the dG-TLIH technique is superior to that of the model established using a fixed TLIH of 450 km. Among them, the model accuracy improves most significantly in low latitude regions, followed by high latitude regions. In mid-latitude regions, the method proposed in this paper is slightly superior to the fixed TLIH model. This phenomenon is consistent with the temporal and spatial characteristics of the ionospheric variations, especially in low latitude regions where the ionospheric activity is very intense and equatorial anomalies exist, making the ionospheric gradient in this region more prominent (Huang et al. 2019). In high latitude regions, the ionospheric variations are influenced by the interplanetary magnetic field, solar wind, and geomagnetic field, resulting in complex changes (Xi et al. 2020). However, compared to low latitude regions, the electron density in this region is generally smaller. Compared to a fixed TLIH, TLIH determined based on the dG-TLIH technique better fits the actual ionospheric spatial gradient, thereby effectively improving the accuracy of the ionospheric models. Compared to high- and low-latitude regions, the ionosphere in mid-latitude regions is less variable, and even with a fixed TLIH, it is possible to construct a good ionospheric TEC model.

We conducted specific numerical statistics on Fig. 8, as shown in Table 1. According to the table, the average bias of the ionospheric model based on the TLIH from the dG-TLIH technique is approximately 0.09 TECU, -0.12 TECU, and 0.01 TECU during the entire test period in low, middle, and high latitudes. On the other hand, the average bias for the fixed TLIH is approximately 0.14 TECU, -0.14 TECU, and 0.00 TECU. Compared to the ionospheric model based on the fixed TLIH of 450 km, the new model shows a reduction in RMS errors of 0.49 TECU, 0.06 TECU, and 0.11 TECU in the low, middle, and high latitudes, respectively. This translates to an improvement of about 16.3%, 9.6%, and 14.8% across the three latitude regions.

### TLIH effects on satellite and receiver DCBs

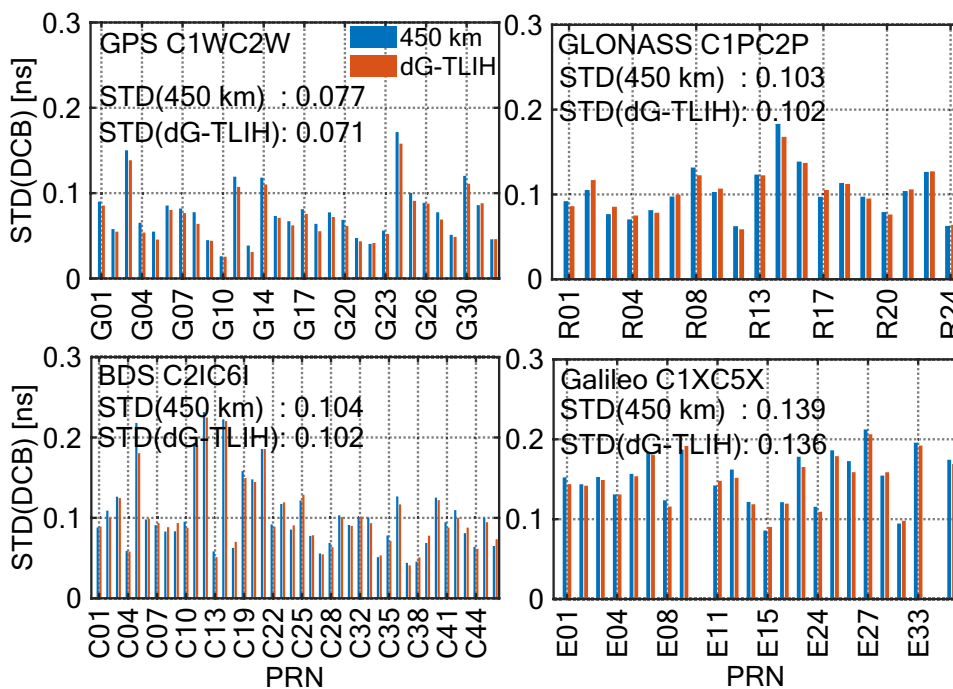
To verify the impact of TLIH determined by the dG-TLIH technique on the accuracy of DCB estimation, we estimated

**Table 1** Statistical results of ionospheric TEC models for different TLIHs using dSTEC measurements in different latitudes

Region	TLIH		dG-TLIH		Improvement (%)
	450 km				
	Bias	RMS	Bias	RMS	
Low-Lat	0.14	2.95	0.09	2.47	16.3
Mid-Lat	-0.14	1.36	-0.11	1.23	9.6
High-Lat	0.01	1.49	0.02	1.27	14.8

The units of the bias and RMS are TECU

**Fig. 9** The standard deviation (STD) errors for GPS C1WC2W DCB, GLONASS C1PC2P DCB, BDS C2IC6I DCB and Galileo C1XC5X DCB derived from two TLIHs during DOY 80 to 89 in 2022. The blue bar represents the results using the TLIH of 450 km and the red bar represents the results using the TLIH from dG-TLIH technique



satellite and receiver DCBs (GPS C1WC2W, GLONASS C1PC2P, BDS C2IC6I, Galileo C1XC5X) using the IGG-DCB algorithm based on different TLIHs and global IGS observation stations (as shown in Fig. 1). Figure 9 shows the standard deviation (STD) errors ( $STD = \sqrt{\frac{1}{n-1} \sum_{i=1}^n (DCB_i - \overline{DCB})^2}$ ,  $n$  is the number of samples;  $DCB_i$  is the sample of satellite or receiver DCBs;  $\overline{DCB}$  is the mean of the same satellite or receiver DCB during the experimental period) of four types of satellite DCB derived from two TLIHs (450 km and dG-TLIH) during DOY 80 to 89 in 2022. The blue bar represents the results using the TLIH of 450 km and the red bar represents the results using the TLIH from the dG-TLIH technique. It can be observed that during the testing period, except for some Beidou-2 satellites whose DCB standard deviation exceeds 0.2 ns, the DCB standard deviation of the remaining satellites is generally within 0.2 ns. Overall, the stability of GPS C1WC2W DCB is the best, the STD of BDS C2IC6I DCB is similar to that of GLONASS C1PC2P DCB, and the STD of Galileo C1XC5X DCB is relatively larger. One of the factors that significantly affects the stability of DCB is the quantity of available observation data. Compared to the other three types of DCB, there are relatively fewer receivers that are capable of receiving Galileo C1X and C5X data. This may also result in a larger standard deviation for C1XC5X DCB. In addition, we can also see that the stability of DCB estimated based on TLIH from the dG-TLIH technique is slightly better than that of using a fixed TLIH of 450 km.

In order to evaluate the accuracy of external conformity of GPS, GLONASS, BDS, and Galileo satellites, as well as receiver DCB estimates, the products from the Multi-GNSS Experiment (MGEX) provided by the Chinese Academy of Sciences (CAS) are used as reference values. Figure 10 illustrates the differences between the daily DCB estimates of the four types of satellites (GPS C1WC2W DCB, GLONASS C1PC2P DCB, BDS C2IC6I DCB, and Galileo C1XC5X DCB) obtained from different TLIHs and those obtained from MGEX. For comparison purposes, the DCB estimates of the four types based on the TLIH obtained from the dG-TLIH technique are also compared with the MGEX values. The differences are highlighted in red in Fig. 10. Similarly, the DCB values based on the fixed TLIH of 450 km were compared with those from the MGEX product. As shown in the figure, it is evident that the DCB estimates of most satellites based on the TLIH derived from the dG-TLIH technique have improved compared to those derived from the fixed TLIH of 450 km. Using the TLIH from the dG-TLIH technique, Fig. 10 indicates that the C1WC2W DCB differences of most GPS satellites range from 0 to 0.3 ns, the C1PC2P DCB differences of most GLONASS satellites range from -0.2 to 0.2 ns, the C2IC6I DCB differences of most BDS satellites range from -0.3 to 0.3 ns, and the C1XC5X DCB differences of most Galileo satellites range from -0.15 to 0.15 ns.

The bias and RMS errors of differences between the GPS, GLONASS, BDS, and Galileo satellite DCB estimates derived from two kinds of TLIH and the reference values from MGEX are listed in Table 2. It can be observed that the



**Fig. 10** The differences between the daily satellite DCB estimates derived from two TLIHs and the daily DCB values from the CAS during DOY 80 to 89 in 2022. The blue bar represents the results using the TLIH of 450 km and the red bar represents the results using the TLIH from dG-TLIH technique

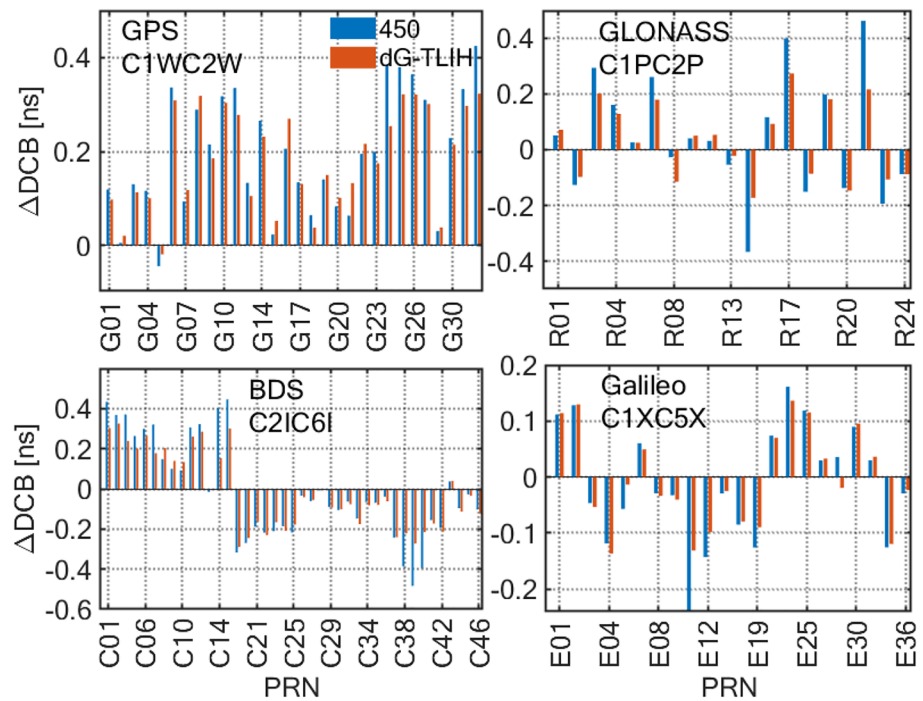


**Table 2** Statistical results of satellite DCBs relative to the daily DCB products from the CAS for different TLIHs

Indicators	DCB type							
	C1WC2W		C1PC2P		C2IC6I		C1XC5X	
	Bias	RMS	Bias	RMS	Bias	RMS	Bias	RMS
450 km	0.21	0.24	0.22	0.24	0.23	0.27	0.14	0.15
dG-TLIH	0.19	0.21	0.18	0.19	0.19	0.22	0.14	0.14
Improvement (%)	9.5	12.5	18.2	20.8	17.4	18.5	0.00	6.7

The units of the bias and RMS are TECU

**Table 3** Statistical results of receive DCBs relative to the MGEX DCB products for different TLIHs

DCB type	TLIH				Improvement (%)
	450 km		dG-TLIH		
	Bias	RMS	Bias	RMS	
C1WC2W	-0.27	0.66	-0.22	0.61	7.6
C1PC2P	-0.12	0.73	-0.06	0.64	12.3
C2IC6I	-0.07	0.71	0.03	0.60	15.5
C1XC5X	0.01	0.74	-0.03	0.66	10.8

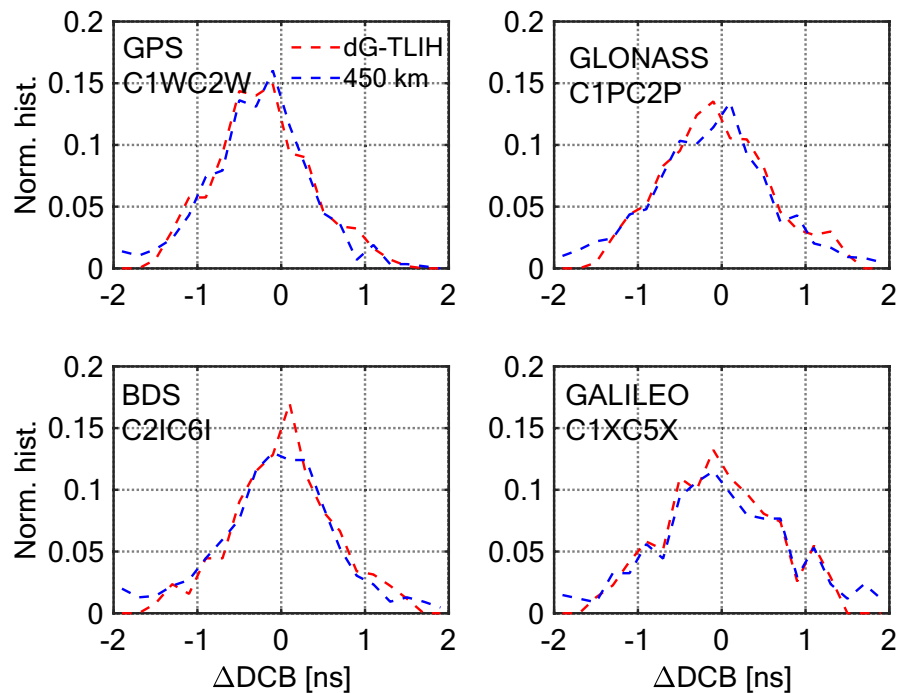
The units of the bias and RMS are TECU

bias and RMS errors of all four types of DCB based on TLIH derived from the dG-TLIH technique are better than 0.20 ns and 0.22 ns, respectively. This indicates that the proposed algorithm can generate accurate estimates of satellite DCBs. Table 3 also indicates that the C1WC2W, C1PC2P, C2IC6I, and C1XC5X DCB values obtained using the dG-TLIH

algorithm have improved by an average of 12.5%, 20.8%, 18.5%, and 6.7%, respectively.

Furthermore, we conducted a detailed statistical analysis for the four types of receiver DCBs. The normalized histograms of the differences between the four types of receiver daily DCBs (GPS C1WC2W DCB, GLONASS C1PC2P DCB, BDS C2IC6I DCB, and Galileo C1XC5X DCB) estimates obtained from different TLIHs and those obtained from MGEX DCB products are shown in Fig. 11. The total number of selected C1WC2W, C1PC2P, C2IC6I, and C1XC5X receiver DCBs is 557, 1072, 763, and 310, respectively. As shown in the figure, the four types of receiver DCB bias essentially follow a normal distribution with a mean value of zero. The bias of the four DCB types is predominantly distributed between ± 2.0 ns. Figure 11 also indicates that the bias distribution of receiver DCB based on TLIH from the dG-TLIH technique is more peaked compared to DCB based on the fixed TLIH of 450 km.

**Fig. 11** Histograms of the daily receiver DCB errors relative to the DCB from the CAS for different TLIHs during the DOY 80 to 89 in 2022. The blue dashed line represents the results using the TLIH of 450 km and the red dashed line represents the results using the TLIH from dG-TLIH technique



The Bias and RMS errors of differences between the GPS, GLONASS, BDS and Galileo receiver DCB estimates derived from two kind of TLIH and the reference values from MGEX DCB products are listed in Table 3. We can observe that the average deviation of most receiver DCBs is negative. This is because the receiver and satellite DCB are linearly correlated, and the satellite DCB deviation is mostly positive (as shown in Table 2), so the receiver DCB deviation is mostly negative. Using the TLIH derived from dG-TLIH technique, the RMS errors of four types of receiver DCB are ranged from 0.6 to 0.7 ns. Compared to the fixed TLIH of 450 km, the C1WC2W, C1PC2P, C2IC6I and C1XC5X receiver DCB values using the dG-TLIH algorithm are improved by an average of 7.6, 12.3, 15.5 and 10.8%, respectively.

## Summary and conclusions

In the process of converting slant TEC to vertical TEC, inevitable mapping errors are introduced. In order to reduce the impact of these mapping errors on the modeling of ionospheric TEC and improve the estimation accuracy of DCB, we propose a single-station ionospheric modeling method based on the dG-TLIH technique and apply it to DCB estimation. This method aims to optimize the modeling of ionospheric TEC to reduce the influence of mapping errors and thus improve the accuracy of DCB estimation.

The contributions of the paper include the analysis of the spatio-temporal variation of the mapping function and the thin layer height using the dG-TLIH technique. Using

ionospheric observables based on CCL, we analyzed impacts of the two TLIHs on the single-station ionospheric TEC modeling, satellite and receiver DCB estimation. The specific conclusions are as follows:

- (1) The “true” mapping value is closely related to latitude and local time. Although with an increasing elevation angle, the mapping value under different ionospheric conditions tends to be 1, there is still a possibility of a 0.1 deviation in mapping value when the elevation reaches  $40^\circ$ . Therefore, using only a fixed TLIH is difficult to reflect the “true” mapping value.
- (2) The TLIH exhibits obvious diurnal variations. During the day, as the sun rises, photoionization begins, causing TLIH to decrease rapidly. When the sun sets, TLIH starts to rise and reaches its peak between 4:00 and 5:00. However, in the polar regions, TLIH exhibits different variations from those in middle and low latitude regions due to the combined effects of factors such as polar day, the interplanetary magnetic field, and the geomagnetic field.
- (3) Compared to the single-station ionospheric TEC model based on the fixed TLIH of 450 km, the RMS errors of the model based on the TLIH derived from dG-TLIH technique are reduced by 0.48 TECU, 0.13 TECU and 0.22 TECU and improved by about 16.3%, 9.6%, and 14.8% in the low, middle and high latitudes, respectively.
- (4) For satellite and receiver DCB estimation, the GPS C1WC2W, GLONASS C1PC2P, BDS C2IC6I and Galileo C1XC5X satellite DCB values using the dG-

TLIH technique are improved by an average of 12.5, 20.8, 18.5 and 6.7%, respectively. The receiver DCB values are improved by an average of 7.6, 12.3, 15.5 and 10.8%, respectively.

According to the characteristics of the dG-TLIH technique, it can be understood that the reliability of the “true” mapping values depends on the GIM model used. Due to the large coverage of satellites observed by the GNSS station, the TLIH may not have been accurate enough to cover a large area. In addition, the conclusions of this study should be used with caution due to the limited amount of test data.

**Acknowledgements** The authors would like to acknowledge the International GNSS Services (IGS) for providing access to the GNSS observations and DCB products. Our deepest gratitude goes to Professor Manuel Hernández-Pajares for his guidance in dG-TLIH technique. This research was funded by the Shandong Provincial Natural Science Foundation (Grant Nos. ZR2022QD109, ZR2021QD152), by the State Key Laboratory of Geodesy and Earth's Dynamics, Innovation Academy for Precision Measurement Science and Technology, CAS (Grant No. SKLGED2024-3-4) and the National Natural Science Foundation of China (Grant No. 42230104).

**Author contributions** Conceptualization, H.J.; Methodology, H.J. and J.A.; Software, H.X.; Validation, J.B. and N.C.; Formal analysis, H.X. and J.A.; Investigation, H.X.; Resources, H.J.; Data curation, H.J.; Writing—original draft preparation, H.J., H.X.; Writing—review and editing, H.X. and T.B.; Visualization, H.X.; Supervision, H.J.; Funding acquisition, H.X. All authors have read and agreed to the published version of the manuscript.

**Data availability** No datasets were generated or analysed during the current study.

## Declarations

**Conflict of interest** The authors declare that they have no conflict of interest.

## References

- Birch MJ, Hargreaves JK, Bailey GJ (2002) On the use of an effective ionospheric height in electron content measurement by GPS reception. *Radio Sci* 37(1):1–19. <https://doi.org/10.1029/2000rs002601>
- Chen P, Wang R, Yao Y, An Z, Wang Z (2022) A novel ionospheric mapping function modeling at regional scale using empirical orthogonal functions and GNSS data. *J Geodesy* 96(5):1–12. <https://doi.org/10.1007/s00190-022-01624-x>
- Ciraolo L, Azpilicueta F, Brunini C, Meza A, Radicella S (2007) Calibration errors on experimental slant total electron content (TEC) determined with GPS. *J Geod* 81(2):111–120
- Hernández-Pajares M, Juan JM, Sanz J, Aragón-Ángel À, García-Rigo A, Salazar D, Escudero M (2011) The ionosphere: effects, GPS modeling and the benefits for space geodetic techniques. *J Geodesy* 85(12):887–907. <https://doi.org/10.1007/s00190-011-0508-5>
- Horvath I (2006) A total electron content space weather study of the nighttime Weddell Sea Anomaly of 1996/1997 southern summer with TOPEX/Poseidon radar altimetry. *J Geophys Res* 111(A12):99–103
- Huang F, Otsuka Y, Lei J, Luan X, Dou X, Li G (2019) Daytime periodic wave-like structures in the ionosphere observed at low latitudes over the Asian-Australian sector using total electron content from Beidou geostationary satellites. *J Geophys Res-Space* 124(3):2312–2322. <https://doi.org/10.1029/2018JA026443>
- Jiang H, Wang Z, An J, Liu J, Wang N, Li H (2018) Influence of spatial gradients on ionospheric mapping using thin layer models. *GPS Solut* 22(1):2. <https://doi.org/10.1007/s10291-017-0671-0>
- Jiang H, Liu J, Wang Z, An J, Ou J, Liu S, Wang N (2019) Assessment of spatial and temporal TEC variations derived from ionospheric models over the polar regions. *J Geodesy* 93(4):455–471. <https://doi.org/10.1007/s00190-018-1175-6>
- Jiang H, Jin S, Hernandez-Pajares M, Xi H, An J, Wang Z, Xu X, Yan H (2021) A new method to determine the optimal thin layer ionospheric height and its application in the polar regions. *Remote Sens* 13(13):2458. <https://doi.org/10.3390/rs13132458>
- Jin S, Wang Q, Dardanelli G (2022) A review on multi-GNSS for earth observation and emerging applications. *Remote Sens* 14(16):3930. <https://doi.org/10.3390/rs14163930>
- Klobuchar JA (1987) Ionospheric time-delay algorithm for single-frequency GPS users. *IEEE Trans Aerosp Electron Syst* 23(3):325–331. <https://doi.org/10.1109/taes.1987.310829>
- Komjathy A (1997) Global ionospheric total electron content mapping using the Global Positioning System. In: Ph. D. dissertation, department of geodesy and geomatics engineering, University of New Brunswick, Fredericton, New Brunswick, Canada, pp. 248
- Krankowski A, Shagimuratov II, Ephishov II, Krypiak-Gregorczyk A, Yakimova G (2009) The occurrence of the mid-latitude ionospheric trough in GPS-TEC measurements. *Adv Space Res* 43(11):1721–1731. <https://doi.org/10.1016/j.asr.2008.05.014>
- Li Z, Yuan Y, Li H, Ou J, Huo X (2012) Two-step method for the determination of the differential code biases of COMPASS satellites. *J Geodesy* 86(11):1059–1076. <https://doi.org/10.1007/s00190-012-0565-4>
- Li Z, Yuan Y, Fan L, Huo X, Hsu H (2014) Determination of the differential code bias for current BDS satellites. *IEEE T Geosci Remote* 52(7):3968–3979. <https://doi.org/10.1109/tgrs.2013.2278545>
- Li Z, Yuan Y, Wang N, Hernandez-Pajares M, Huo X (2015) SHPTS: towards a new method for generating precise global ionospheric TEC map based on spherical harmonic and generalized trigonometric series functions. *J Geodesy* 89(4):331–345. <https://doi.org/10.1007/s00190-014-0778-9>
- Li M, Yuan Y, Zhang B, Wang N, Li Z, Liu X, Zhang X (2018) Determination of the optimized single-layer ionospheric height for electron content measurements over China. *J Geodesy* 92(2):169–183. <https://doi.org/10.1007/s00190-017-1054-6>
- Liu J, Chen R, Wang Z, Zhang H (2011) Spherical cap harmonic model for mapping and predicting regional TEC. *GPS Solut* 15(2):109–119. <https://doi.org/10.1007/s10291-010-0174-8>
- Liu J, Chen R, An J, Wang Z, Hyyppä J (2014) Spherical cap harmonic analysis of the Arctic ionospheric TEC for one solar cycle. *J Geophys Res-Space* 119(1):601–619. <https://doi.org/10.1002/2013JA019501>
- Liu J, Hernandez-Pajares M, Liang X, An J, Wang Z, Chen R, Sun W, Hyyppä J (2016) Temporal and spatial variations of global ionospheric total electron content under various solar conditions. *J Geodesy* 91(5):485–502. <https://doi.org/10.1007/s00190-016-0977-7>
- Macalalad EP, Tsai L-C, Wu J (2014) Performance evaluation of different ionospheric models in single-frequency code-based differential GPS positioning. *GPS Solut* 20(2):173–185. <https://doi.org/10.1007/s10291-014-0422-4>
- Nava B, Radicella SM, Leitinger R, Coisson P (2007) Use of total electron content data to analyze ionosphere electron density gradients. *Adv Space Res* 39(8):1292–1297. <https://doi.org/10.1016/j.asr.2007.01.041>

- Rovira-Garcia A, Juan JM, Sanz J, Gonzalez-Casado G (2015) A worldwide ionospheric model for fast precise point positioning. *IEEE T Geosci Remote* 53(8):4596–4604. <https://doi.org/10.1109/TGRS.2015.2402598>
- Sasibhushana Rao G (2007) GPS satellite and receiver instrumental biases estimation using least squares method for accurate ionosphere modelling. *J Earth Syst Sci* 116(5):407–411. <https://doi.org/10.1007/s12040-007-0039-x>
- Schaer S (1999) Mapping and predicting the earth's ionosphere using the global positioning system. Institut für Geodäsie und Photogrammetrie. Eidg. Technische Hochschule Zürich, Zürich
- Shi C, Fan L, Li M, Liu Z, Gu S, Zhong S, Song W (2016) An enhanced algorithm to estimate BDS satellite's differential code biases. *J Geodesy* 90(2):161–177. <https://doi.org/10.1007/s00190-015-0863-8>
- Wang N, Yuan Y, Li Z, Montenbruck O, Tan B (2016) Determination of differential code biases with multi-GNSS observations. *J Geodesy* 90(3):209–228
- Xi H, Jiang H, An J, Wang Z, Xu X, Yan H, Feng C (2020) Spatial and temporal variations of polar ionospheric total electron content over nearly thirteen years. *Sensors* 20(2):540. <https://doi.org/10.3390/s20020540>
- Xiang Y, Gao Y (2019) An enhanced mapping function with ionospheric varying height. *Remote Sens* 11(12):1497. <https://doi.org/10.3390/rs11121497>
- Xu L, Gao J, Li Z, Shu M, Yang X, Zhang G (2023) A new flexible model to calibrate single-layer height for ionospheric modeling using a neural network model. *GPS Solut* 27(3):106. <https://doi.org/10.1007/s10291-023-01450-4>
- Yuan Y, Ou J (2004) A generalized trigonometric series function model for determining ionospheric delay. *Prog Nat Sci* 14(11):1010–1014. <https://doi.org/10.1080/10020070412331344711>
- Yuan Y, Wang N, Li Z, Huo X (2019) The BeiDou global broadcast ionospheric delay correction model (BDGIM) and its preliminary performance evaluation results. *Navigation* 66(1):55–69. <https://doi.org/10.1002/navi.292>
- Zhang BC (2016) Three methods to retrieve slant total electron content measurements from ground-based GPS receivers and performance assessment. *Radio Sci* 51(7):972–988. <https://doi.org/10.1002/2015rs005916>
- Zhao J, Zhou C (2018) On the optimal height of ionospheric shell for single-site TEC estimation. *GPS Solut* 22(2):1–11. <https://doi.org/10.1007/s10291-018-0715-0>

**Publisher's Note** Springer Nature remains neutral with regard to jurisdictional claims in published maps and institutional affiliations.

Springer Nature or its licensor (e.g. a society or other partner) holds exclusive rights to this article under a publishing agreement with the author(s) or other rightsholder(s); author self-archiving of the accepted manuscript version of this article is solely governed by the terms of such publishing agreement and applicable law.



**Hui Xi** received the B.S. degree in surveying engineering from Shandong University of Technology, Zibo, China, in 2013, and the Ph.D. degree in 2019 at Institute of Geodesy and Geophysics, CAS. She is currently a lecturer in the College of Geography and Environment, Shandong Normal University. Her research interest is GNSS positioning and climate change.



**Hu Jiang** received the M.S. degree at Institute of Geodesy and Geophysics, CAS, in 2016, and the Ph.D. degree at Chinese Antarctic Center of Surveying and Mapping, Wuhan University in Wuhan, China, in 2019. He is currently a lecturer in the School of Surveying and Geo-Informatics, Shandong Jianzhu University in Jinan, China. His current work focuses on ionospheric modeling and GNSS positioning.



**Jiachun An** received the B.Eng. degree in surveying engineering from Southeast University, Nanjing, China, in 2006, and the Ph.D. degree in geodesy and surveying engineering from Wuhan University, Wuhan, China, in 2011. He is currently an associate Professor with the Chinese Antarctic Center of Surveying and Mapping, Wuhan University. He has been working on ionospheric and atmospheric sensing, and global navigation satellite system reflectometry over polar region.





**Na Cheng** received her Ph.D. degree from Shanghai Astronomical Observatory, Chinese Academy of Sciences in 2019. She is currently working in School of Surveying and Geo-Informatics, Shandong Jianzhu University, Jinan, China. Her research focuses on ionospheric modeling and ionospheric anomaly monitoring.



**Jingxue Bi** received the M.S. degree from Shandong University of Science and Technology, Qingdao, China, in 2015, and the Ph.D. degree from China University of Mining and Technology, Xuzhou, China, in 2019. He is currently an associate Professor at Shandong Jianzhu University. His current research interests include indoor positioning and indoor navigation, GNSS application, and human activity recognition.



**Tianyang Bai** is currently a GNSS algorithm engineer at State Grid Siji Location Co., Ltd. He obtained his master's degree from Hohai University, and his current main research direction is GNSS high-precision positioning and ionospheric modeling.